Published in final edited form as:
J Am Chem Soc. 2008 March 19; 130(11): 3509–3515. doi:10.1021/ja0774414.

Probing Electron Correlations in Molecules by Two-Dimensional Coherent Optical Spectroscopy

Zhenyu Li[†], **Darius Abramavicius**, and **Shaul Mukamel**[*]
Department of Chemistry, University of California, Irvine, California 92697

Abstract

The nonlinear optical signal generated in phenol by three femtosecond pulses with wavevectors $\mathbf{k}_1$, $\mathbf{k}_2$, and $\mathbf{k}_3$ in the phase-matching direction $\mathbf{k}_1 + \mathbf{k}_2 - \mathbf{k}_3$ is simulated. This two-dimensional coherent spectroscopy (2DCS) signal has a rich pattern containing information on double-excitation states. The signal vanishes for uncorrelated electrons due to interference among quantum pathways and, thus, provides direct signatures of correlated many-electron wavefunctions. This is illustrated by the very different 2DCS signals predicted by two levels of electronic structure calculations: state-averaged complete active space self-consistent field (SA-CASSCF) and multistate multiconfigurational second-order perturbation theory (MS-CASPT2).

1. Introduction

Computing electron correlations is one of the central challenges of electronic structure theory.[1–3] At the Hartree–Fock (HF) level, the wave function assumes the form of a single Slater determinant, which is antisymmetric with respect to electron exchange. The probability of finding two electrons with parallel spins at the same point in space thus vanishes (Pauli exclusion). This type of correlation which exists at the HF level is commonly denoted as exchange. The correlation energy of a molecule is defined as the difference between the actual and the HF energy. HF method is the reference point of most quantum chemistry calculations. It is easy to show that the restricted HF method cannot describe the dissociation of molecules into open-shell fragments, e.g., $H_2 \rightarrow 2H$. This is because weak or broken bonds involve a large occupation of antibonding orbitals, which cannot be described by a single determinant. This type of correlation, which is essential for the correct asymptotic behavior at long distances, is known as static correlation. The remaining, dynamic correlation, is associated with the instantaneous short-range electron–electron interactions.

Electron correlation effects are crucial for predicting many molecular properties with high accuracy. For example, uncorrelated HF calculations tend to underestimate bond lengths. Static electron correlation increases the antibonding occupations, leading to too long bond lengths. Only when both static and dynamic correlations are included, we get a closer agreement with experiment. It will thus be highly desirable to develop direct experimental probes for electron correlations. Ideally, such signals should vanish for uncorrelated systems and could thus provide a background-free measure of correlations.

[*]smukamel@uci.edu .
[†]Current address: Hefei National Laboratory for Physical Sciences at Microscale, University of Science and Technology of China, Hefei, Anhui 230026, China.

Supporting Information Available: The optimized geometry and total energy of phenol molecule, the expressions for the 2D signals, and the complete citation of ref [22]. This material is available free of charge via the Internat at http://pubs.acs.org. JA0774414

A two-dimensional electronic correlation spectroscopy (2DCS) signal, which has precisely this property, has been proposed recently for semiconductor quantum dots.[4] Multidimensional techniques have had remarkable success in NMR by probing correlations between coherently excited spins. These techniques provide detailed and specific information on the geometry and dynamics of complex molecules. In recent years, these ideas have been extended to femtosecond laser spectroscopy.[5] Infrared techniques probe correlations among the amide vibrations in proteins,[6] and visible pulses probe exciton dynamics in aggregates such as photosynthetic complexes[7,8] and in semiconductor quantum wells.[9] The proposed technique uses four femtosecond pulses with wavevectors $\mathbf{k}_1$, $\mathbf{k}_2$, $\mathbf{k}_3$, and $\mathbf{k}_4 = \mathbf{k}_1 + \mathbf{k}_2 - \mathbf{k}_3$ and detects the heterodyne signal along $\mathbf{k}_4$. This technique which involves double-excitation states has been proven useful for electronic and vibrational excitons.[10–15] Most recently, we have demonstrated that this pulse sequence can be used to directly probe electron correlations.[4] Since the signal vanishes at the uncorrelated level, it provides a novel, unusually sensitive, probe for electron correlations.

In this paper we demonstrate the power of this technique by high-level electronic structure calculations of a simple molecule, phenol. Quantum chemistry techniques for ground state properties are well developed. Excited-state properties are more difficult to calculate. We shall use methods which can treat the ground and excited states in a balanced way. There are two types of approaches for the electronic structure of excited states. The first is the propagator approach (also known as Green's function, equation-of-motion, or linear response theory), which treats the excited states by perturbing the ground electronic state by the electromagnetic field. These techniques strongly depend on the quality of ground state calculation. Time-dependent density functional theory (TDDFT) is a popular example of such methods.

The other class of approaches are wave function based. Starting with a HF ground state wavefunction given by a Slater determinant of molecular orbitals (MOs), one can construct excited states by promoting one or more electrons from an occupied to an unoccupied orbital. With the independent particle Hamiltonian (IPH), the excited-state energies are given by differences of orbital energies. In this uncorrelated HF–IPH picture, the transition energy of a double-excitation state is simply given by the sum of the corresponding two single-excitation energies.

A more rigorous description is configuration interaction singles (CIS),[16] where the excited states are expressed as linear combinations of all singly excited determinants formed by replacing an occupied by an unoccupied orbital. Here, the ground state is still described by the HF Slater determinant, and all excitations are based on this reference configuration. Considering only singly excited determinants may be a serious approximation. Linear combination of all possible excited determinants (full configuration interaction, FCI) gives the most accurate wavefunction for a specific atomic basis set. However, such calculations are only feasible for very small systems, since the time and memory requirements grow exponentially with size. For large molecules, they can be carried out only by restricting the calculation to a small active space. The molecular orbitals should then be optimized together with the CI coefficients. This type of multiconfigurational self-consistent field (MCSCF) method is denoted a complete active space self-consistent field (CASSCF).[17] To obtain good orbitals for both ground state and excited states, CASSCF is usually performed by minimizing the average energy of a few states of interest. This is known as state averaged (SA) CASSCF.

CASSCF describes the static correlations very well and usually generates an optimal set of MOs together with reasonable ground and excited state wavefunctions. Dynamic correlations can be further included by multireference configuration interaction (MRCI) or a multiconfigurational perturbation theory. In MRCI, the CI expansion comprises all configurations that can be generated by single and double excitations from the CASSCF

reference configurations. MRCI is only feasible in relatively small molecules such as benzene. Furthermore, it is not size-extensive. Dynamic correlations can be alternatively included perturbatively. Moller–Plesset second-order perturbation theory (MP2) for ground states with a single determinant reference function has been extended to multiple reference functions of the CAS type, and it is called the CASPT2 method.[18–20] For systems with a strong interaction between different CASSCF wave functions, an effective Hamiltonian can be constructed for several selected states, and the multistate (MS) CASPT2 energies can be then obtained by diagonalizing this Hamiltonian.[21]

We shall employ transition energies and dipoles obtained by two levels of theory, SA-CASSCF and the higher-level MS-CASPT2, to simulate the electronic absorption and 2DCS spectra. The 2DCS signals show projections of the correlated doubly excited wavefunctions onto the manifold of singly excited states. They are very different for the two levels of theory, reflecting the different levels where correlations are treated by the two techniques.

The remainder of this article is organized as follows. In section 2, we introduce the computational methods. The excited states and the linear absorption of phenol are presented in section 3. The 2DCS technique is described in section 4, and the simulated signals are shown in section 5. Finally, we conclude in section 6.

2. Computational Methods

The geometry of phenol, optimized at the B3LYP/6-311++G** level of density functional theory (DFT) using the Gaussian 03 package,[22] is shown in Figure 1. The ground state and excited states electronic structures were then calculated at the SA-CASSCF/MS-CASPT2 levels using the MOLCAS 7.0 package[23] and an atomic natural orbital (ANO) basis set.[24] For heavy atoms, the primitives were contracted to triple-ζ plus polarization quality (4s3p1d), and for hydrogen atoms, the contraction was of double-ζ plus polarization (2s1p) quality. This basis set was further augmented with a set of off-atom diffuse functions for Rydberg states. Following Roos et al.,[25] the following steps were performed in order to obtain these Rydberg basis functions. First, a CASSCF calculation was performed for the phenol cation, and the charge center was set to the center of the Rydberg basis functions. This calculation was then repeated with a (8s8p8d) basis set for Rydberg states[26] added. Finally, Rydberg orbitals were generated using the GENANO program in the MOLCAS package. The orbital coefficients were used as contraction coefficients of the final (1s1p1d) Rydberg basis set.

The quality of the CASSCF calculation depends crucially on the chosen active space. Since the low-energy excitations of phenol are π to π^* transitions, we included all π orbitals and electrons in our active space. With C_s symmetry, this leads to eight electrons in seven *a”* orbitals. However, for small molecules in the gas phase, Rydberg and valence excited-state energies are very close. Rydberg states should thus be also included in the active space. An earlier study had indicated that the Rydberg-valence mixing in phenol is weak.[27] The following strategy was therefore used in order to exclude the Rydberg orbitals from the active space. First, the *sp* Rydberg orbitals were included in the active space. A CASSCF calculation was performed, and the optimized Rydberg states were then deleted. The *d* Rydberg states were optimized and deleted in the same way. The final seven active orbitals which have no Rydberg character are shown in Figure 1.

Within this active space, the lowest 20 *A’* singlet states were calculated at the SA-CASSCF level, where the CI and MO coefficients are optimized to minimize the average energy of the 20 states. An MS-CASPT2 calculation was then performed to include dynamical correlations. The modified zeroth-order Hamiltonian[28] with a IPEA shift of 0.25 hartree was used. A 0.3 hartree level-shift was also employed to eliminate the intruder states. The transition moments

between the 20 states are calculated by the CAS state interaction (CASSI) method[29] implemented in the RASSI program in the MOLCAS package. At the MS-CASPT2 level, perturbatively modified CASSCF wave functions and MS-CASPT2 energies are used for the CASSI calculation.

Using these transition energies and dipoles, the spectra were simulated by the sum over states (SOS) response function expressions[30,31] implemented in the SPECTRON package.[32] The line shape is obtained by cumulant expansion of the Gaussian fluctuation (CGF) formula using an overdamped Brownian oscillator spectral density.[30] We used a bath temperature of 300 K and time scale of 1 ps. The coupling parameter was set to give a Gaussian profile with a $\sigma = 200$ cm^{-1} variance. An average over all possible orientations of the molecule was performed during the spectra simulations.

3. Excited States and the Linear Absorption of Phenol

The excited states of phenol have been extensively studied, both theoretically[27,33,34] and experimentally.[35–38] The first two singlet excited states mainly correspond to transitions from the highest occupied molecular orbital HOMO (H) to the lowest unoccupied molecular orbital LUMO (L), and L+1. Their corresponding Platt's notation[39] is L_b and L_a, where the subscripts refer to the transition dipole orientation, *a* for the long axis and *b* for the short axis. These two states are the analogues of the B_{2u} and B_{1u} states of benzene. The leading configuration of the next two excited states B_b and B_a are H−1 to L+1 and to L. These are the analogues of the E_{1u} states of benzene.

Some properties of the six lowest excited states are listed in Table 1. The first three excited-state energies calculated by MS-CASPT2 are ~0.3 eV higher than the experimental absorption peaks. We note that the vertical excitation energies for the first two excited states of benzene are 0.1 eV higher than the absorption band maxima.[40] Assuming a similar blue shift between vertical excitation energy and absorption band maxima for phenol, the actual difference between theory and experiment is ~0.2 eV. We aim toward a balanced description for the low single-excitation and higher double-excitation states. For higher excited states, a much larger active space will be required. Therefore, an MS-CASPT2 calculation only for low-energy excited states will give better agreement with experiment. Our test MS-CASPT2 calculation with the current active space but only for the lowest seven states (7S-CASPT2 in Table 1) gives good agreement with experiment.

The higher excited states are listed in Table 2. Most of them are dominated by double-excitation configurations. The SA-CASSCF states more strongly mix different configurations. Unlike the lowest six excited states, there is no one-to-one map between SA-CASSCF and MS-CASPT2 for the higher states based on their main configurations. This implies that double-excitation states are more sensitive to electron correlations and their calculation is more challenging.

A good indicator of electron correlations is the anharmonicity parameter, defined as the difference of the transition energy of a double-excitation state and the sum of the two corresponding single-excitation states. The anharmonicity vanishes for uncorrelated electrons, where excitation energies are additive. For phenol, the 2H → L, L+1 state, which is a combined state of the first two single-excitation states (L_b and L_a), can be clearly identified by both SA-CASSCF (10*A*') and MS-CASPT2 (11*A*'). The predicted anharmonicities are −0.57 and −0.62 eV, respectively.

The absorption spectra are displayed in Figure 2. In addition to SA-CASSCF and MS-CASPT2, we also show two additional levels of theory. One is TDDFT (B3LYP/6-311G**), where the diffusion functions were excluded from the basis set to avoid valence Rydberg mixing. Within

the adiabatic approximation, it contains correlations but not double-excitation states.[41,42] The other is the uncorrelated HF–IPH model, where the ground state wavefunction was calculated at the HF/6-311G** level. The HF–IPH transition dipoles were obtained by calculating the dipole integral between two single determinants. The lowest two peaks in all spectra correspond to the L_b and L_a states. As shown in Table 3, the TDDFT and MS-CASPT2 calculations give relatively good excitation energies compared to experiment, and HF–IPH strongly overestimate the excitation energies. TDDFT predicts a stronger L_b peak, in contrast to experiment and to SA-CASSCF and MS-CASPT2. Both HF–IPH and TDDFT underestimate the energy splitting between L_b and L_a. SA-CASSCF overestimates it, and MS-CASPT2 is in a very good agreement with experiment.

The absorption spectra provide some valuable information about correlations through the peak positions and intensities. In the next section, we shall demonstrate how 2DCS provide a much more detailed look into the correlated many-body wavefunctions.

4. 2DCS Signal Induced by Electron Correlations

The proposed experiment shown in Figure 3 uses four laser pulses with wavevectors $\mathbf{k}_1$, $\mathbf{k}_2$, $\mathbf{k}_3$, and $\mathbf{k}_4 = \mathbf{k}_1 + \mathbf{k}_2 - \mathbf{k}_3$. The signal is defined as the change in the $\mathbf{k}_4$ beam transmitted intensity due to the interference with the induced nonlinear polarization. This configuration, known as heterodyne detection, can be viewed as a stimulated four-wave mixing signal.[43] We assume an impulsive experiment with temporally well-separated pulses. The molecule-field interaction is $-\widehat{V}E(\mathbf{r},t)$, where $\widehat{V}$ is the dipole operator, and the field is expanded as

$$E(\mathbf{r},t)=\sum_{j}^{4}\epsilon_j\left(t-\tau_j\right)e^{i\mathbf{k}_j\mathbf{r}-i\omega_j\left(t-\tau_j\right)}+\epsilon_j^{*}\left(t-\tau_j\right)e^{-i\mathbf{k}_j\mathbf{r}+i\omega_j\left(t-\tau_j\right)} \tag{1}$$

where the jth pulse is centered at time τ_j and has an envelope $\epsilon_j(t-\tau_j)$, carrier frequency ω_j, and wavevector $\mathbf{k}_j$. The consecutive time delays between the pulses in chronological order are denoted t_1, t_2, and t_3.

The signal is given by

$$\begin{aligned} I^{(3)}(\tau_4 &, \tau_3, \tau_2, \tau_1 = -\operatorname{Im}\int_{-\infty}^{\infty}d\bar{\tau}_4\int_{-\infty}^{\bar{\tau}_4}d\bar{\tau}_3\int_{-\infty}^{\bar{\tau}_3}d\bar{\tau}_2\int_{-\infty}^{\bar{\tau}_2}d\bar{\tau}_1 R^{(3)}\left(\bar{\tau}_4\right. \\ &, \bar{\tau}_3, \bar{\tau}_2, \bar{\tau}_1 \times \epsilon_4^{*}\left(\bar{\tau}_4\right. \\ &- \tau_4\epsilon_3^{*}\left(\bar{\tau}_3\right. \\ &- \tau_3\epsilon_2\left(\bar{\tau}_2\right. \\ &- \tau_2\epsilon_1\left(\bar{\tau}_1\right. \\ &- \tau_1 \times e^{+i\omega_4\bar{\tau}_4+i\omega_3\bar{\tau}_3-i\omega_2\bar{\tau}_2-i\omega_1\bar{\tau}_1} \end{aligned} \tag{2}$$

where the response function $R^{(3)}$ is given by a combination of the four-time correlation functions of the dipole operator $\widehat{V}(\tau)$, which can be calculated by the sum-over-states expression.[30] In principle, the entire complex manifold of excited states must be included in computing $R^{(3)}$. However, in practice, only some groups of states are relevant for resonant

signals. These states can be controlled by selecting the phase-matching direction ($\mathbf{k}_4$), the carrier frequencies, and the pulse bandwidths, as will be explained below. For simplicity, in our simulations, we assumed the same carrier frequencies for all pulses $\omega_1 = \omega_2 = \omega_3 = \omega_4 \equiv \omega_0$ and used rectangular spectral envelopes for all pulses. ω_0 was fixed in the middle of the two peaks in the linear absorption. For MS-CASPT2 excited states, this gives four pulses centered at 5.5 eV with a bandwidth $\Delta = 2$ eV. For SA-CASPT2, the four pulses are centered at 6.1 eV with $\Delta = 3$ eV. With this pulse configuration, as shown in Figure 4a, the first two MS-CASPT2 excited states of phenol, L_b and L_a, correspond to one photon energy. They are single-excitation states, denoted by $|e\rangle$.

The signal generated in the $\mathbf{k}_1 + \mathbf{k}_2 - \mathbf{k}_3$ direction has two contributions, represented by the double-sided Feynman diagrams[30] *A* and *B*, shown in Figure 5. These diagrams represent the resonant contributions which dominate the signal. In both diagrams, the molecule first absorbs an ω_1 photon, which brings it to state $|e\rangle$. The density matrix element $|e\rangle\langle g|$ oscillates at frequency ω_{eg}. The accessible $|e\rangle$ state must lie in the region $\omega_0 \pm \Delta/2$ allowed by the pulse bandwidth. Pulse $\mathbf{k}_2$ is then absorbed and brings $|e\rangle$ to one of the states $|f\rangle$ in the region $2\omega_0 \pm \Delta$. The density matrix element $|f\rangle\langle g|$ oscillates at frequency ω_{fg}. So far, the sequence of events is the same for both diagrams *A* and *B*. The two differ however by the action of the third pulse. In *A*, it stimulates an emission bringing the molecule to a state $|e'\rangle$ in the region $\omega_0 \pm \Delta/2$. In *B*, a photon is absorbed bringing the density matrix to an $|f\rangle\langle e'|$ coherence which oscillates at the $\omega_{fe'}$ frequency.

There are two ways to define double-excitation states. Using the electronic structure, these are excited states whose dominant configuration has two electrons promoted from occupied to unoccupied molecular orbitals. Spectroscopically, any state located in the two-photon energy region $\omega_1 + \omega_2 \pm \Delta$ is denoted a double-excitation state. Its contribution to the spectrum is determined by its transition dipole from the lower single-excitation states. For uncorrelated electrons with zero anharmonicity, these two definitions coincide. As shown in Figure 4b, in this case, the double-excitation states are combinations of two single-excitation states, and the corresponding excitation energy is the sum of the two single-excitation energies.

We define the multidimensional signal by the triple Fourier transform

$$S^{(3)}(\Omega_3,\Omega_2,\Omega_1) = \int\int\int_0^\infty \mathrm{d}t_3\,\mathrm{d}t_2\,\mathrm{d}t_1\, e^{i\Omega_1 t_1 + i\Omega_2 t_2 + i\Omega_3 t_3} \times I^{(3)}(t_1+t_2+t_3, t_1+t_2, t_1, 0) \tag{3}$$

For well-separated pulses, the signal is given by[44]

$$S^{(3)}(\Omega_3,\Omega_2,\Omega_1) = \sum_{e,e',f} \frac{\epsilon_1(\omega_1-\omega_{eg})\,\epsilon_2(\omega_2-\omega_{fe})\,\epsilon_3^*(\omega_{fe'}-\omega_3)\,\epsilon_4^*(\omega_{e'g}-\omega_4)\,V_{ge'}V_{e'f}V_{fe}V_{eg}}{(\Omega_3-\omega_{e'g}+i\Gamma_{e'g})(\Omega_2-\omega_{fg}+i\Gamma_{fg})(\Omega_1-\omega_{eg}+i\Gamma_{eg})}$$
$$- \sum_{e,e',f} \frac{\epsilon_1(\omega_1-\omega_{eg})\,\epsilon_2(\omega_2-\omega_{fe})\,\epsilon_3^*(\omega_{e'g}-\omega_3)\,\epsilon_4^*(\omega_{fe'}-\omega_4)\,V_{e'f}V_{fe}V_{eg}V_{ge'}}{(\Omega_3-\omega_{fe'}+i\Gamma_{fe'})(\Omega_2-\omega_{fg}+i\Gamma_{fg})(\Omega_1-\omega_{eg}+i\Gamma_{eg})} \tag{4}$$

where $\epsilon_j(\Omega_j) = \int \mathrm{d}t\ \epsilon_j(t)\, e^{i\Omega_j t}$, $\omega_{\mu\nu} \equiv E_\mu - E_\nu$ is the frequency, $\Gamma_{\mu\nu}$ is the dephasing rate of the transition between states ν and μ, and $\omega_4 = \omega_1 + \omega_2 - \omega_3$. The two terms correspond, respectively, to diagrams *A* and *B*.

By holding ω_1, ω_2, and ω_3 fixed (this selects the relevant energy range) and calculating the signal versus Ω_1, Ω_2, and Ω_3, we obtain a three-dimensional signal. We shall present the signal

in two types of two-dimensional plots. The first is (Ω_1, Ω_2) for a fixed t_3. Note that this signal vanishes for $t_3 = 0$. The second is (Ω_3, Ω_2) for a fixed t_1. By varying the time delay t_3 for the (Ω_1, Ω_2) signal or t_1 for the (Ω_3, Ω_2) signal, we can extract information about electron dynamics.

As shown in Figure 4b, for uncorrelated electrons, the transition energy of a double-excitation state will be equal to the sum of the corresponding two single-excitation states. For a double-excitation state $|f\rangle = |e_1e_1\rangle$, $e = e' = e_1$ in both diagram *A* and *B*. We have $\omega_{e'g} = \omega_{fe'} = \omega_{ge1}$, and the two diagrams exactly cancel, and thus $S^{(3)} = 0$. For the excited state $|f\rangle = |e_1e_2\rangle$, the cancellation of *A* and *B* is more subtle. Setting $e = e_1$, then e' will be either e_1 or e_2 for a harmonic system without correlation. If we chose $e' = e_1$ in diagram *A*, it will be canceled by diagram *B* with $e' = e_2$. This can be easily shown by noting that $\omega_{e1g} = \omega_{fe2}$. Similarly, if $e' = e_2$ in diagram *A* and $e' = e_1$ in diagram *B*, they also cancel. Therefore, the entire 2DCS signal is induced by electron correlations and Vanishes for uncorrelated systems.

5. 2DCS of Phenol

The simulated (Ω_1, Ω_2) signal for $t_3 = 1$ fs is shown in Figure 6. SA-CASSCF and MS-CASPT2 show a rich and clearly distinct peak pattern. The contributions from diagrams *A* and *B* are similar for each quantum chemistry level. Generally, the MS-CASPT2 signal, which includes higher level electron correlations, shows more peaks. The Ω_1 axis represents the single-excitation states. Two single-excitation states L_b and L_a are accessible by our pulse bandwidths, yielding a two-stripe pattern for the 2DCS signal. The Ω_2 axis represents the double-excitation states. These are clearly seen. Generally, transitions from L_a to double-excitation states are stronger than transitions from L_b. The strongest MS-CASPT2 peak corresponds to the transition from L_a to the 2H–1 → 2L state (15*A*'). The strongest SA-CASSCF peak is from the same transition (L_a to 14*A*'). It is interesting to note that the strongest peaks in our 2D signals do not come from the combination state of L_b and L_a (2H → L, L+1). This indicates that electron correlations in phenol are very strong and the level scheme is highly anharmonic.

A notable advantage of 2DCS is its ability to provide direct information on the *many-body correlated wavefunction* of double-excitation states, by looking at the relative strength of peaks representing transitions from different single-excitation states. Let us consider the MS-CASPT2 double-excitation state at 12.32 eV (17*A*'). It has a much stronger transition from L_b than from L_a. This can be easily understood by looking at its configuration coefficients. The main configuration of 17 *A*' is H–1, H → 2L, which is a combination of H–1 → L and H → L (L_b). For systems with weak anharmonicity, such as photosynthetic complexes described by the Frenkel exciton model, it is possible to directly extract the main configuration of the double-excitation states by this type of analysis.[45]

The (Ω_3, Ω_2) signal displayed in Figure 7 is more complex. The contribution of diagram *A* is similar to that in Figure 6. However, diagram *B* leads to a more complicated signal. Since the Ω_3 axis now represents transition energies between single-and double-excitation states $\omega_{fe'}$, the signal does not show a simple two-stripe pattern.

Even though both 2D signals are induced by correlation, they carry a different information. The $S^{(3)}(t_3, \Omega_2, \Omega_1)$ signal is simpler and directly reveals the energies of the relevant single- and double-excitation states. With this information, combined with wavefunction projection analysis from both $S^{(3)}(\Omega_3, \Omega_2, t_1)$ and $S^{(3)}(t_3, \Omega_2, \Omega_1)$ signals, we obtain additional information about the excited state wavefunction.

6. Conclusions and Discussion

A novel two-dimensional coherent spectroscopy technique has been demonstrated to provide a direct probe of electron correlations in phenol. The signals obtained using excited states calculated at the SA-CASSCF and MS-CASPT2 levels are compared. The former only includes static correlations, whereas the latter contains dynamic correlations as well. The 2DCS signals predicted by these two levels of theory are very different. This signal provides information about transition energies of double-excitation states, as well as their many-body correlated wavefunctions. The ability to measure double-excitation states directly can provide a new experimental test for the accuracy of the electron correlations described in different levels of theory and offers a way for visualizing some projections of the many-electron wavefunctions. Since an excited configuration is a molecular-orbital-based concept, we do not expect to unambiguously determine the excited configurations experimentally, especially for molecules with a strong mixing between singly and doubly excited configurations. However, we can obtain some useful information about the excited-state wavefunction by analyzing the projections of the two-excitation state onto the single-excitation states.

To simplify the simulations and generate the entire spectrum in a single calculation, we have used unphysically broad pulse bandwidth (2 eV for MS-CASPT2 and 3 eV for SA-CASSCF) in the 2DCS signal simulation. In practice, the predicted signal can be observed piecewise by multiple measurements obtained by scanning the carrier frequencies over the entire frequency range. In fact, any three states $|e\rangle$, $|e'\rangle$, and $|f\rangle$ can be probed tuning the carrier frequencies of the four pulses. By combining spectra obtained with various carrier frequencies, it should be possible to reconstruct the signal simulated here. When the pulses are tuned to $\omega_4 \approx \omega_{e'g}$, $\omega_3 \approx \omega_{fe'}$, $\omega_2 \approx \omega_{ef}$, and $\omega_1 \approx$ we obtain the (ω_{eg}, ω_{fg}, $\omega_{e'g}$) peaks corresponding to diagram *A*. The peaks (ω_{eg}, ω_{fg}, $\omega_{fe'}$) from diagram *B* will be probed with $\omega_4 \approx \omega_{fe'}$, $\omega_3 \approx \omega_{e'g}$, $\omega_2 \approx \omega_{ef}$, and $\omega_1 \approx \omega_{ge}$. Attosecond X-ray pulses have much broader bandwidths(e.g., 1 eV for 1 fs pulse).[46,47] X-ray Raman techniques[44] could thus probe the entire 2D signal in a single shot.

It should be noted that the cancellation predicted here is purely electronic. Coupling to other degrees of freedom (vibrations and dephasing induced by solvent) can affect different excited states differently and may break the exact cancellation. This could result in weak new features.

Finally, we note that, in addition to the $\mathbf{k}_1 + \mathbf{k}_2 - \mathbf{k}_3$ signal discussed here, the 2DCS signal in the $\mathbf{k}_1 + \mathbf{k}_2 + \mathbf{k}_3$ direction also vanishes for uncorrelated electron systems. The sum-over-states expression of the signal is (see diagram *C* in Figure 5)

$$S_h^{(3)}(\Omega_3,\Omega_2,\Omega_1)=\sum_{e,f,h}\frac{\epsilon_1\left(\omega_1-\omega_{eg}\right)\epsilon_2\left(\omega_2-\omega_{fe}\right)\epsilon_3\left(\omega_3-\omega_{hf}\right)\epsilon_4^*\left(\omega_{hg}-\omega_4\right)V_{gh}V_{hf}V_{fe}V_{eg}}{\left(\Omega_3-\omega_{hg}+i\Gamma_{hg}\right)\left(\Omega_2-\omega_{fg}+i\Gamma_{fg}\right)\left(\Omega_1-\omega_{eg}+i\Gamma_{eg}\right)} \quad (5)$$

where the summation runs over single-excitation states $|e\rangle$, double-excitation states $|f\rangle$, and triple-excitation states $|h\rangle$ According to the Condon–Slater rules, the transition dipole between two Slater determinants which differ by two or more orbitals is zero. Therefore, for uncorrelated electrons, $V_{gh} = 0$. Three excitations bring the molecule to a three quantum coherence, and a dipole moment V_{gh} is required to bring it back to a population and generate a signal. The signal $S^{(3)}{}_h$ thus vanishes for uncorrelated electrons. In this case however, there is only one pathway; the vanishing of the signal is not caused by the destructive interference between two pathways. $S^{(3)}{}_h$ could probe electron correlations corresponding to both double excitations and triple excitations.

Supplementary Material

Refer to Web version on PubMed Central for supplementary material.

Acknowledgments

We wish to thank Prof. B. O. Roos for help in using the MOLCAS package. This work was supported by the National Institutes of Health Grant GM59230 and the National Science Foundation Grant CHE-0446555.

References

(1). Fulde, P. Electron Correlations in Molecules and Solids. 3rd ed. Springer-Verlag; Berlin: 1995.

(2). Olivucci, M., editor. Computational Photochemistry. Elsevier; Amsterdam: 2005.

(3). Wilson, AK.; Peterson, KA., editors. Recent Advances in Electron Correlation Methodology. American Chemical Society; Washington, DC: 2007.

(4). Mukamel S, Oszwaldowski R, Yang L. J. Chem. Phys 2007;127:221105. [PubMed: 18081382]

(5). Mukamel S. Ann. Rev. Phys. Chem 2000;51:691. [PubMed: 11031297]

(6). Zanni MT, Hochstrasser RM. Curr. Opin. Struct. Biol 2001;11:516. [PubMed: 11785750]

(7). Lee H, Cheng Y-C, Fleming GR. Science 2007;316:1462. [PubMed: 17556580]

(8). Engel GS, Calhoun t. R. Read EL, Ahn T-K, Mancal T, Cheng YC, Blankenship RE, Fleming GR. Nature 2007;446:782. [PubMed: 17429397]

(9). Li X, Zhang T, Borca CN, Cundiff ST. Phys. Rev. Lett 2006;96:57406.

(10). Leegwater JA, Mukamel S. J. Chem. Phys 1994;101:7388.

(11). Kuhn O, Chernyak V, Mukamel S. J. Chem. Phys 1996;105:8586.

(12). Scheurer C, Mukamel S. J. Chem. Phys 2001;115:4989.

(13). Mukamel S, Tortschanoff A. Chem. Phys. Lett 2002;357:327.

(14). Cervetto V, Helbing J, Bredenbeck J, Hamm P. J. Chem. Phys 2004;121:5935. [PubMed: 15367022]

(15). Fulmer EC, Mukherjee P, Krummel AT, Zanni MT. J. Chem. Phys 2004;120:8067. [PubMed: 15267726]

(16). Foresman JB, Head-Gordon M, Pople JA, Frisch MJ. J. Phys. Chem 1992;96:135.

(17). Roos BO, Taylor PR. Chem. Phys 1980;48:157.

(18). Andersson K, Malmqvist P-A, Roos BO. J. Chem. Phys 1992;96:1218.

(19). Andersson K, Roos BO. Chem. Phys. Lett 1992;191:507.

(20). Roos BO, Andersson K, Fulscher MP. J. Chem. Phys 1992;192:5.

(21). Finley J, Malmqvist P-A, Roos BO, Serrano-Andres L. Chem. Phys. Lett 1998;288:299.

(22). Frisch, MJ., et al. Gaussian 03. Gaussian, Inc.; Wallingford, CT: 2004. revision C.02

(23). Karlstrom G, Lindh R, Malmqvist P-A, Roos BO, Ryde U, Veryazov V, Widmark P-O, Cossi M, Schimmelpfennig B, Neogrady P, Seijo L. Comput. Mater. Sci 2003;28:222.

(24). Widmark P-O, Malmqvist P-A, Roos BO. Theor. Chim. Acta 1990;77:291.

(25). Roos, BO.; Fulscher, MP.; Malmqvist, P-A.; Merchan, M.; Serrano-ANdres, L. Quantum Mechanical Electronic Structure Calculations with Chemical Accuracy. Kluwer Academic Publisers; Dordrecht: 1995. p. 357-438.

(26). Kaufmann K, Baumeister W, Jungen M. J. Phys. B: At. Mol. Opt. Phys 1989;22:2223.

(27). Rogers DM, Hirst JD. J. Phys. Chem. A 2003;107:11191.

(28). Ghigo G, Roos BO, Malmqvist PA. Chem. Phys. Lett 2004;396:142.

(29). Malmqvist P-A, Roos BO. Chem. Phys. Lett 1989;155:189.

(30). Mukamel, S. Principles of Nonlinear Optical Spectroscopy. Oxford University Press; New York: 1995.

(31). Mukamel S, Abramavicius D. Chem. Rev 2004;104:2073. [PubMed: 15080721]

(32). Zhuang W, Abramavicius D, Hayashi T, Mukamel S. J. Phys. Chem. B 2006;110:3362. [PubMed: 16494351]

(33). Lorentzon J, Malmqvist P-A, Fulscher M, Roos BO. Theor. Chim. Acta 1995;91:91.
(34). Zhang L, Peslherbe GH, Muchall H. Photochem. Photobiol 2006;82:324. [PubMed: 16313201]
(35). Martinez SJ III, Alfano JC, Levy DH. J. Mol. Spectrosc 1992;152:80.
(36). Kimura L, Nagakura S. Mol. Phys 1965;9:117.
(37). Ratzer C, Kupper J, Spangenberg D, Schmitt M. Chem. Phys 2002;283:153.
(38). Dearden JC, Forbes WF. Can. J. Chem 1956;37:1294.
(39). Platt JR. J. Chem. Phys 1949;17:484.
(40). Bernhardsson A, Forsberg N, Malmqvist PA, Roos BO, Serrano-Andres L. J. Chem. Phys 2000;112:2798.
(41). Maitra NT, Zhang F, Cave RJ, Burke K. J. Chem. Phys 2004;120:5932. [PubMed: 15267474]
(42). Casida M. J. Chem. Phys 2005;122:54111. [PubMed: 15740314]
(43). Marx C, Harbola U, Mukamel S. Phys. Rev. A. 2008 in press.
(44). Schweigert, IV.; Mukamel, S. Unpublished
(45). Abramavicius, D.; Mukamel, S.; Voronine, DV. Unpublished
(46). Goulielmakis E, Yakovlev VS, Cavalieri AL, Uiberacker M, Pervak V, Apolonski A, Kienberger R, Kleineberg U, Krausz F. Science 2007;317:769. [PubMed: 17690286]
(47). Kapteyn H, Cohen O, Christov I, Murnane M. Science 2007;317:775. [PubMed: 17690287]

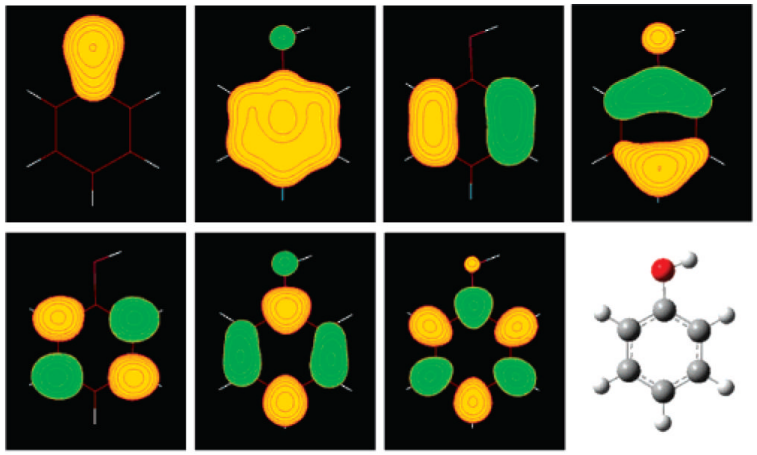

Figure 1.
Active orbitals 1*a*” to 4*a*” (top row) and 5*a*” to 7*a*” (second row) used in our simulations of phenol. 4*a*” is the HOMO, and 5*a*” is the LUMO. The last panel shows the optimized geometry.

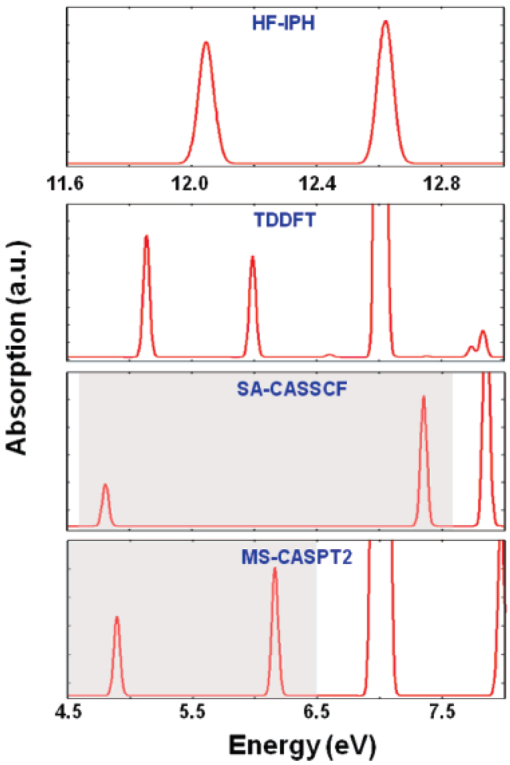

Figure 2.
Simulated absorption spectrum for phenol in the gas phase. Energy ranges 4.6 to 7.6 eV in the SA-CASSCF spectrum and 4.5 to 6.5 eV in the MS-CASPT2 spectrum. Shadowed areas mark the spectral region covered by the pulse bandwidths.

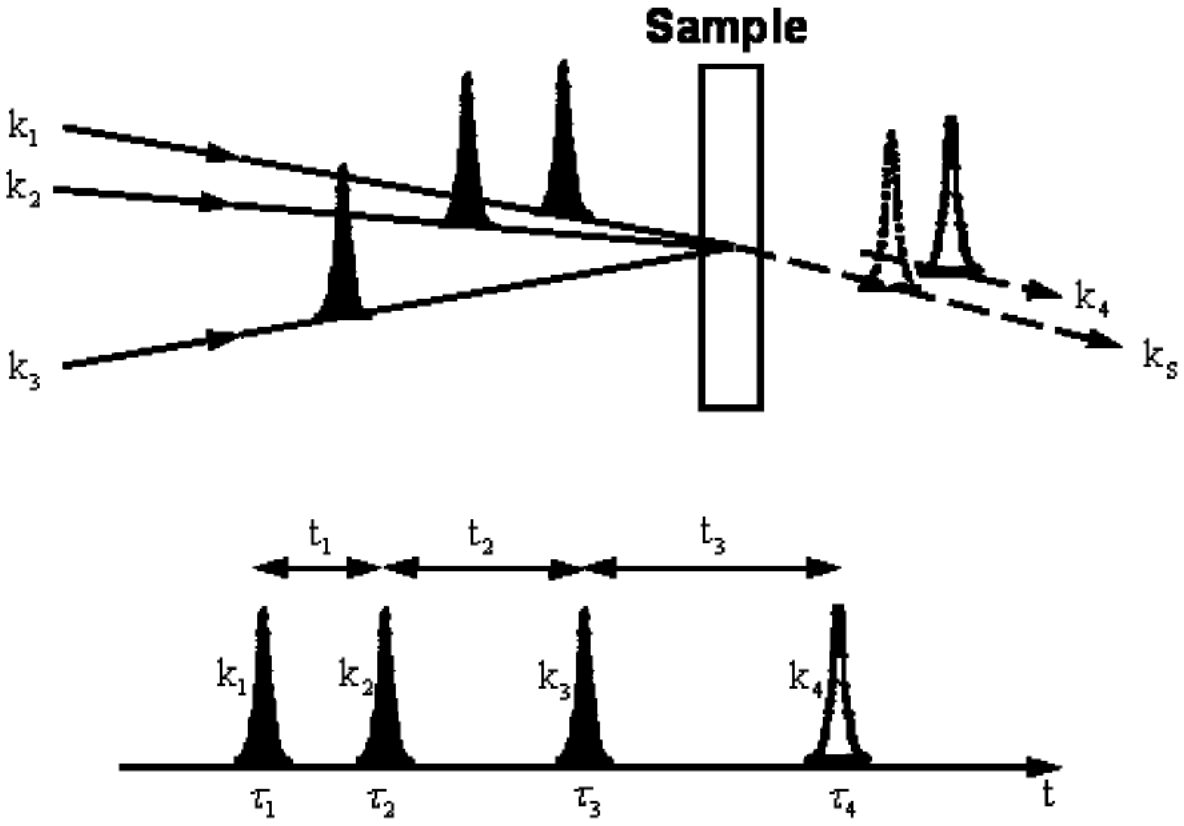

Figure 3.
Top panel: Pulse configuration for 2DCS. $\mathbf{k}_1$, $\mathbf{k}_2$, and $\mathbf{k}_3$ are the input pulses. The signal is generated along the detection pulse $\mathbf{k}_4$. Bottom panel: The pulse sequence. t_j are the time intervals between pulses centered at τ_i.

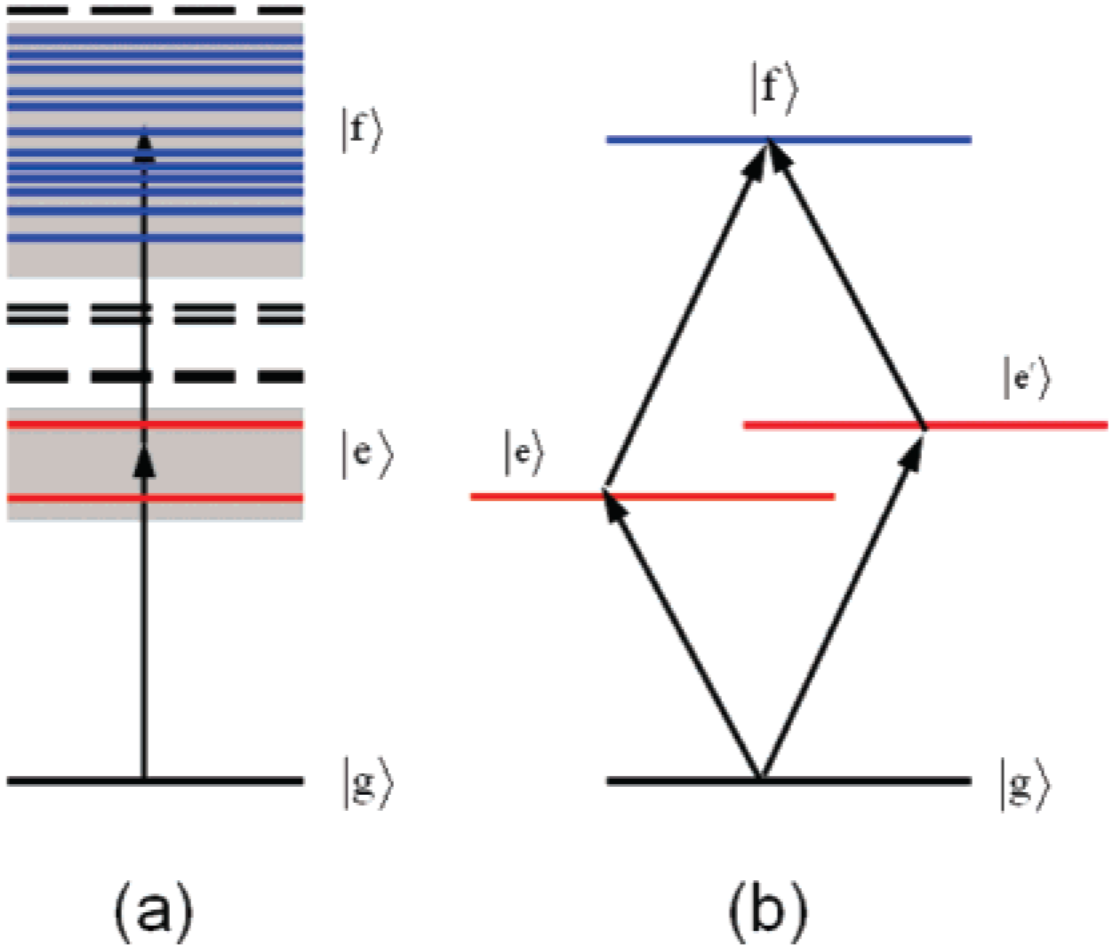

Figure 4.

(a) Many-body states of phenol, including the ground state $|g\rangle$ (black), the manifold of single-excitation states $|e\rangle$ (red), and the manifold of double-excitation states $|f\rangle$ (blue). States off-resonant with fields are marked by dash lines. The shadow areas mark the energy range covered by pulse bandwidths for single- and double-photon absorption. (b) Schematic level model for an uncorrelated (harmonic) system.

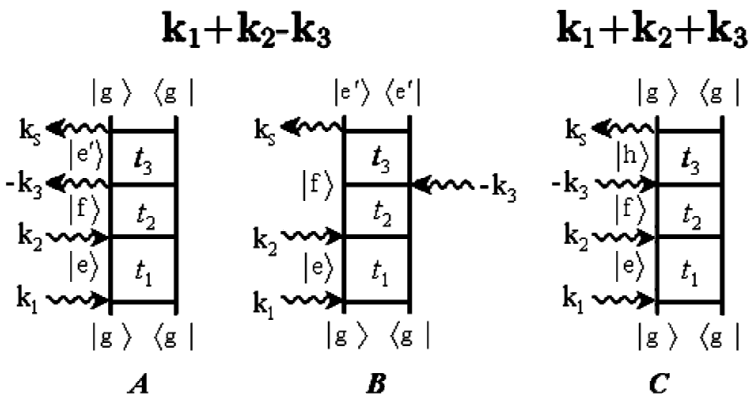

Figure 5.

(A and B) The two double sided Feynman diagrams contributing to the $\mathbf{k}_1 + \mathbf{k}_2 - \mathbf{k}_3$ 2DCS signal. (C) Diagram representing the $\mathbf{k}_1 + \mathbf{k}_2 + \mathbf{k}_3$ 2DCS signal. Both signals are induced by electron correlations.

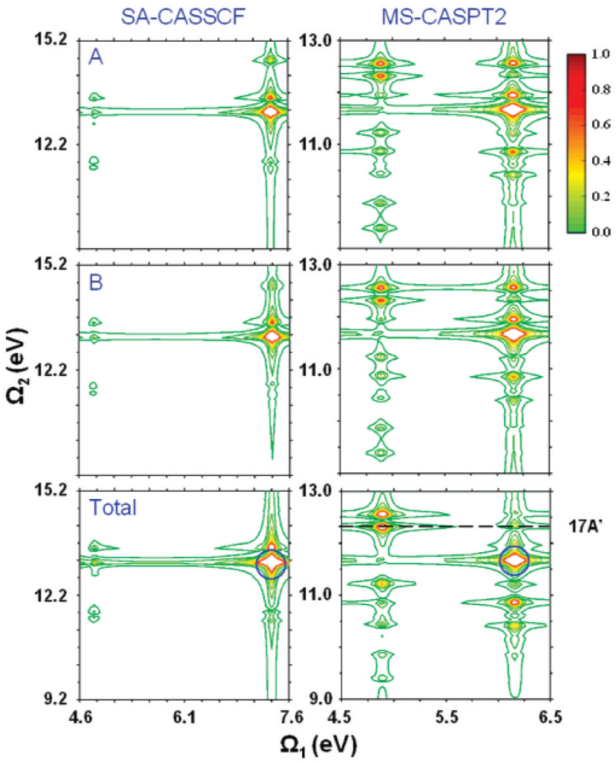

Figure 6.

Simulated $S^{(3)}(t_3, \Omega_2, \Omega_1)$ 2DCS signal (amplitude) of phenol at t_3 = 1 fs. Left column: SA-CASSCF. Right column: MS-CASPT2. From top to bottom, contribution from diagrams *A*,*B* and the total signal. The strongest peak in the total-signal panel is indicated by a blue circle. The MS-CASPT2 double-excitation states, 17*A'*, is marked by a dashed line.

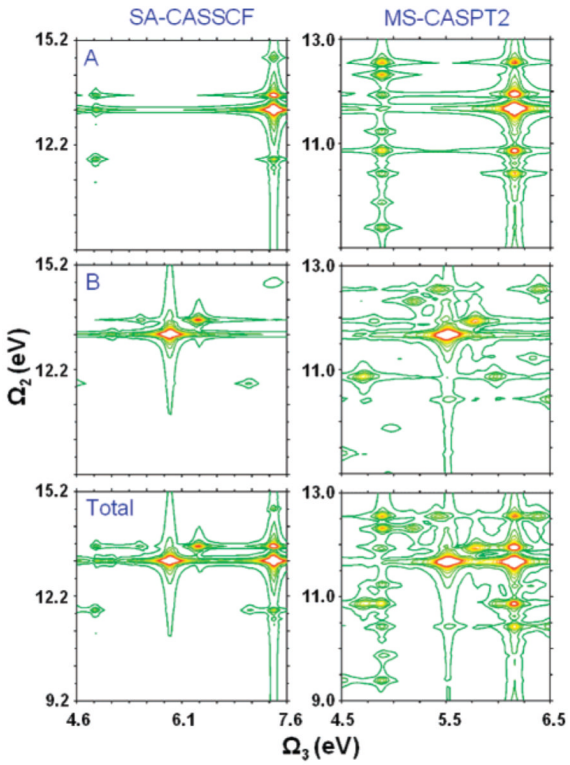

Figure 7.
Simulated $S^{(3)}(\Omega_3, \Omega_2, t_1)$ signal (amplitude) of phenol at $t_1 = 0$. Left panel: SA-CASSCF. Right panel: MS-CASPT2. Contributions from diagrams *A*,*B* and the total signal are shown, from top to bottom. The same color bar as that in Figure 6 is used.

Table 1

Excitation Energies (in eV) of the First Six Excited States of Phenol[a]

	Platt notation	benzene notation	main configuration	SA-CASSCF	MS-CASPT2	7S-CASPT2	expt[36]
2 *A'*	L_b	B_{2u}	H → L	4.81	4.89	4.79	4.59
3 *A'*	L_a	B_{1u}	H → L+1	7.35	6.16	5.93	5.82
4 *A'*	B_b	E_{1u}	H–1 → L+1	8.95	6.96	6.66	6.70
5 *A'*	B_a	E_{1u}	H–1 → L	8.79	7.05	6.80	6.93
6 *A'*		E_{2g}	H–2 → L	7.85	8.00	8.10	
7 *A'*		E_{2g}	H–2 → L+1	8.08	8.19	8.04	

[a]The two columns denoted by SA-CASPSCF and MS-CASPT2 are results from calculations of the first 20 states. 7S-CASPT2 denotes a MS-CASPT2 calculation for the lowest seven states, where a 0.1 hartree level shift was used. States are shown in ascending order of the MS-CASPT2 energies.

Table 2

Higher Excited States[a]

	SA-CASSCF			MS-CASPT2		
	E_x (eV)	**E_a (eV)**	**main configurations**	**E_x (eV)**	**E_a (eV)**	**main configurations**
8 *A'*	11.13		H–1,H → L,L+1; 2H→2L	9.39		H → L+2
9 *A'*	11.43		2H → 2L; 2H–1 → 2L; 2H → 2L+1	9.87		H–3 → L
10 *A'*	11.59	−0.57	2H → L,L+1	10.18		H–1,H → L,L+1
11 *A'*	11.80		H–2 → L+1	10.43	−0.62	2H → L,L+1
12 *A'*	11.82		H–2 → L; H–1 → L+3; 2H → L,L+1	10.63		H–3 → L
13 *A'*	12.82		H–3 → L	10.87		2H → 2L; 2H → 2L+1
14 *A'*	13.22	−4.36	2H–1 → 2L	11.23		H–3 → L+1
15 *A'*	13.32		H–3 → L+1	11.67	−2.43	2H–1 → 2L
16 *A'*	13.62	−2.68	H–1,H → 2L+1	11.94	−1.18	H–1,H → 2L+1
17 *A'*	14.66		2H–1 → 2L+1; 2H → 2L	12.32	0.38	H–1,H → 2L
18 *A'*	14.72		H–1,H → 2L; H–1,H → 2L+1	12.55		H–1,H → 2L; 2H → 2L+1
19 *A'*	15.03		H–2 → L+2	12.82		H–2 → L+2
20 *A'*	16.09		H → L+2; H–1,H → L,L+1	13.34	−0.58	2H–1 → 2L+1

[a] E_X is the transition energy, and E_a is the anharmonicity.

Table 3

Low-Energy Linear Absorption Properties of Phenol[a]

	L_b	L_a	$L_a - L_b$	r
HF–IPH	12.05	12.62	0.57	1.17
TDDFT	5.05	5.81	0.76	0.85
SA-CASSCF	4.81	7.35	2.54	1.81
MS-CASPT2	4.89	6.16	1.27	1.73
expt[36]	4.59	5.82	1.23	6.6

[a] *r* is the intensity ratio of the L_a and L_b transitions. All energies are in eV.